



# 2<sup>nd</sup> Advanced Optical Metrology Compendium

## Advanced Optical Metrology

Geoscience | Corrosion | Particles | Additive Manufacturing: Metallurgy, Cut Analysis & Porosity



**EVIDENT**  
**OLYMPUS**

**WILEY**

The latest eBook from **Advanced Optical Metrology**.  
Download for free.

This compendium includes a collection of optical metrology papers, a repository of teaching materials, and instructions on how to publish scientific achievements.

With the aim of improving communication between fundamental research and industrial applications in the field of optical metrology we have collected and organized existing information and made it more accessible and useful for researchers and practitioners.

**EVIDENT**  
**OLYMPUS**

**WILEY**

# Merging Nanowires and Formation Dynamics of Bottom-Up Grown InSb Nanoflakes

Marco Rossi, Ghada Badawy, Zhi-Yuan Zhang, Guang Yang, Guo-An Li, Jia-Yu Shi, Roy L. M. Op het Veld, Sasa Gazibegovic, Lu Li, Jie Shen,\* Marcel A. Verheijen, and Erik P. A. M. Bakkers\*

Indium Antimonide (InSb) is a semiconductor material with unique properties, that are suitable for studying new quantum phenomena in hybrid semiconductor-superconductor devices. The realization of such devices with defect-free InSb thin films is challenging, since InSb has a large lattice mismatch with most common insulating substrates. Here, the controlled synthesis of free-standing 2D InSb nanostructures, termed as “nanoflakes”, on a highly mismatched substrate is presented. The nanoflakes originate from the merging of pairs of InSb nanowires grown in V-groove incisions, each from a slanted and opposing  $\{111\}$ B facet. The relative orientation of the two nanowires within a pair, governs the nanoflake morphologies, exhibiting three distinct ones related to different grain boundary arrangements: no boundary (type-I),  $\Sigma 3$ - (type-II), and  $\Sigma 9$ -boundary (type-III). Low-temperature transport measurements indicate that type-III nanoflakes are of a relatively lower quality compared to type-I and type-II, based on field-effect mobility. Moreover, type-III nanoflakes exhibit a conductance dip attributed to an energy barrier pertaining to the  $\Sigma 9$ -boundary. Type-I and type-II nanoflakes exhibit promising transport properties, suitable for quantum devices. This platform hosting nanoflakes next to nanowires and nanowire networks can be used to selectively deposit the superconductor by inter-shadowing, yielding InSb-superconductor hybrid devices with minimal post-fabrication steps.

## 1. Introduction

Low-dimensional nanostructures made of InSb have attracted great attention in recent years, thanks to their potential applications. Among all the III-V materials, InSb possesses a narrow bandgap and stands out for its high electron mobility, large Landé g-factor, and strong Rashba spin-orbit coupling, making it a good candidate for applications in spintronics,<sup>[1,2]</sup> infrared detection,<sup>[3–5]</sup> spin-qubits,<sup>[6]</sup> thermoelectric<sup>[7]</sup> and for studying novel quantum transport phenomena in hybrid semiconductor-superconductor devices.<sup>[8–11]</sup> 2D InSb nanostructures, i.e., quantum wells, have shown great potential as a semiconductor platform for such semiconductor-superconductor device hybrids.<sup>[12–15]</sup> InSb quantum wells are, however, difficult to grow epitaxially on insulating substrates, since they require a stack of buffer layers to accommodate the large lattice constant of InSb.<sup>[16–19]</sup> Furthermore, the need for top-down fabrication processes to realize the final device

M. Rossi, G. Badawy, R. L. M. Op het Veld, S. Gazibegovic, E. P. A. M. Bakkers  
Applied Physics and Science Education Department  
Eindhoven University of Technology  
Eindhoven 5600 MB, The Netherlands  
E-mail: e.p.a.m.bakkers@tue.nl

Z.-Y. Zhang, G. Yang, G.-A. Li, J.-Y. Shi, L. Li, J. Shen  
Beijing National Laboratory for Condensed Matter Physics  
Institute of Physics  
Chinese Academy of Sciences  
Beijing 100190, China  
E-mail: shenjie@iphy.ac.cn

Z.-Y. Zhang, G.-A. Li, L. Li  
School of Physical Sciences  
University of Chinese Academy of Sciences  
Beijing 100049, China

L. Li, J. Shen  
Songshan Lake Materials Laboratory  
Dongguan 523808, China

M. A. Verheijen  
Eurofins Materials Science Netherlands B.V.  
High Tech Campus 11  
Eindhoven 5656 AE, The Netherlands

 The ORCID identification number(s) for the author(s) of this article can be found under <https://doi.org/10.1002/adfm.202212029>.

© 2023 The Authors. Advanced Functional Materials published by Wiley-VCH GmbH. This is an open access article under the terms of the Creative Commons Attribution License, which permits use, distribution and reproduction in any medium, provided the original work is properly cited.

DOI: 10.1002/adfm.202212029

may degrade the superior transport properties of the quantum well.<sup>[18,20,21]</sup> A way around these issues is the bottom-up growth of free-standing nanostructures. Free-standing 2D nanostructures can be grown on lattice-mismatched substrates without defects because they efficiently accommodate strain due to their small footprint. For device fabrication, the metal or superconductor can be selectively deposited by inter-shadowing techniques. This selective deposition alleviates the need for etching and fabrication and thus allows for smooth and pristine metal-semiconductor interfaces.<sup>[22–25]</sup> Selective deposition along with the high crystal quality of the InSb platform enable the study of new transport phenomena.

Free-standing 2D InSb nanostructures have been synthesized via Vapor-Liquid-Solid (VLS) growth with a very high crystal quality, showing single-crystalline or nearly single-crystalline nanostructures.<sup>[26–30]</sup> In these studies, the 2D InSb nanostructures are termed nanoflakes, nanosails, or nanosheets and they all have a common aspect: they originate from a single seed particle. However, these studies have little or no control over the position, yield and orientation of the free-standing InSb nanostructures. The lack of control makes these methods not suitable for the fabrication of InSb-based devices via smart-inter-shadowed deposition, where a wisely devised pattern for positioning the 2D InSb nanostructures and other free-standing objects, i.e., InSb nanowires or 2D nanostructures – is at the base of the technique.

In this paper, we introduce a method for growing free-standing 2D InSb nanostructures at pre-determined positions with a preset number (frequency) and a fixed orientation/alignment via Metal-Organic Vapor Phase Epitaxy (MOVPE). This level of control is achieved because our 2D nanostructures – referred to as nanoflakes – grow by merging of two Aucatalyzed InSb nanowires, whose positions are pre-determined. Since the plane of the InSb nanoflakes is spanned by the two InSb nanowires, they all have a fixed orientation, namely the nanoflake plane is perpendicular to the substrate plane. Compared to previous works on the fabrication of free-standing 2D InSb nanostructures, our method allows for the growth of InSb nanowires alongside InSb nanoflakes all with pre-determined positions and orientations, and to create complex shadowing geometries with nanowire networks. These advancements enable more complex device geometries in combination with the directional deposition of a superconductor. Moreover, the InSb nanoflakes grown with this method are thinner compared to those grown via molecular-beam-epitaxy (MBE),<sup>[31]</sup> which makes them transparent to transmission-electron-microscopy (TEM) and helps to achieve the 2D confinement that is necessary to use the nanoflakes as 2D platform for semiconductor-superconductor device hybrids. Here, we investigate the formation mechanism of these nanoflakes and study their transport properties.

## 2. Results and Discussion

To induce a merging event between two InSb nanowires, we position Au seed particles on two opposing slanted facets, exposing {111}B planes that are etched as V-groove incisions (trenches) in an InP(100) wafer (see Figure 1a). The pair of Au seed particles intended for the merging event needs to be

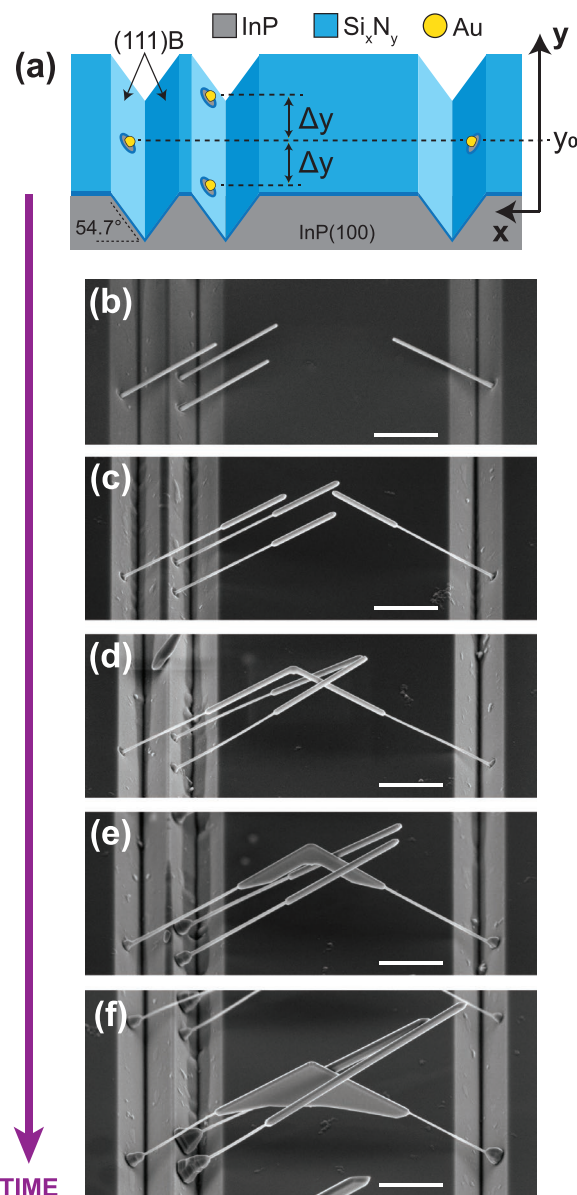


**Figure 1.** a) A schematic of the platform for the growth of InSb nanoflakes and nanowires. A pattern of V-groove incisions (“trenches”) exposing (111)B facets is fabricated on an InP(100) wafer. Au seed particles are lithographically patterned on pre-determined locations of the InP(111)B facets, where the InSb nanowires want to be grown. InSb nanowires are forced to merge by depositing Au seed particles on opposing InP(111)B facets and so that their y-coordinate is the same ( $y_0$  in the sketch). Shadowing, non-merging nanowires can be grown next to a nanoflake on the same or another trench with a minimum offset ( $\Delta y$  in the sketch) given by the final thickness of the InSb nanostructures, to avoid collisions. b–f) A series of scanning electron microscopy (SEM) images showing the time evolution and growth stages going from InP stems up to InSb nanoflakes. b) InP nanowire “stems” grown from the gold particles. c) InSb nanowires grown on top of InP stems. d) Coalescence of the gold particles and merging of two InSb nanowires originating from opposite  $\langle 111 \rangle$ B directions and same y-coordinate, forming a bridging nanostructure. As the growth is further continued, the nanostructure widens along the plane spanned by the two original InSb nanowires by forming e) a nanobridge and then f) a nanoflake. The touching between the non-merging nanowires in d) and f) was induced by the SEM inspection, due to charging effect. All the SEM images are taken at a  $30^\circ$  tilting angle and all scale bars are  $1 \mu\text{m}$ .

positioned without any offset ( $y_0$  in Figure 1a) along a pair of neighboring trenches. We create the trenches using high-temperature etching with HCl gas in a MOVPE reactor.<sup>[32]</sup> This process ensures more control over the etching parameters than standard wet etching techniques and thus leads to a higher reproducibility over the lateral and vertical dimensions of the trenches. Electron beam lithography is used to pattern the Au seed particles on two opposing InP{111}B facets of two neighboring trenches. Au is evaporated within nanoholes that are lithography patterned into a thin silicon nitride ( $\text{Si}_x\text{N}_y$ ) mask. An amorphous  $\text{Si}_x\text{N}_y$  mask enables selective-area VLS growth, i.e., nucleation on the mask is prevented and precursors are restricted to the VLS growth.<sup>[33]</sup> Since Au seed particles are on {111}B facets, the InSb nanowires grow along their preferred <111>B direction, which is perpendicular to the {111}B facets. Moreover, because the {111}B planes are inclined, a pair of nanowires, each growing from an opposing {111}B facets, always grow toward each other ensuring a high yield of merging events. Additional Au seed particles can be deposited in selected positions along the same or another trench, to create shadowing structures that can be used during a directional superconductor deposition. Figure 1a shows a representative sketch of the platform prior the nanowire growth, where two additional Au seed particles are positioned with an offset  $\Delta y$  from the two that are intended for the merging event. A detailed description of the full fabrication process of the platform can be found in Section S1 (Supporting Information).

InSb nanowires are grown as a heterostructure on top of InP nanowires (“stems”). Hence, InP stems are first grown from the Au seed particles (Figure 1b) and then InSb nanowires are grown on top of them (Figure 1c). More details of the nanowire growth can be found in Section S1 (Supporting Information). The two InSb nanowires originating from the pair of Au seed particles aligned without offset will grow toward each other and eventually merge by forming an InSb bridging nanostructure (Figure 1d). For longer growth times, we observe that in most cases this nanostructure develops into a 2D InSb nanostructure that tends to broaden predominantly along the plane formed by the two original InSb nanowires (Figure 1e). Therefore, these nanostructures have a thickness comparable to the diameters of the two original InSb nanowires, which we report to be  $\approx 100 \text{ nm} \pm 20 \text{ nm}$  thin in our growth conditions (see Figure S3 and Section S2, Supporting Information). Evidence of this growth behavior has been observed in merging InSb nanowires grown by MBE<sup>[31]</sup> and MOVPE,<sup>[34]</sup> in contrast to merging InAs nanowires, where the nanowires intersect without forming 2D nanostructures.<sup>[33]</sup> The InSb bridging nanostructure has a concave edge at the bottom, which disappears for longer growth times as a consequence of the 2D broadening (Figure 1e,f). Nanoflakes are defined as InSb nanostructures without a concave edge, meaning that the nanostructure broadened such that the concave edge no longer forms a growth front (Figure 1f). Conversely, InSb nanostructure with a pronounced concave edge at the bottom, we label “nanobridges” (Figure 1e). Multiple nanoflakes and nanowire networks can be grown simultaneously on the same sample with this technique, allowing the fabrication of shadowing designs with high yield (see Figure S4, Supporting Information).

A nanoflake develops as a result of a successful merging event, where two Au particles coalesce into one, implying a tip-to-tip collision between the two nanowires. The relative position of the two Au seed particles on the opposite {111}B facets is crucial for the formation of the InSb nanoflakes. A perfect merging event can occur only if a pair of Au seed particles are perfectly aligned (same y-coordinate in Figure 1a). A very small offset between the two seed particles, i.e., about the diameter of the Au seed particle, will lead to an imperfect merging between the two InSb nanowires yielding two-crossed nanowires instead.<sup>[34,35]</sup>

A second pre-requisite for a tip-to-tip collision is an equal growth rate of the nanowires, which yields reproducible nanoflake morphologies. Conversely, a difference in growth rate will lead to a tip-to-sidewall merging where the two Au seed particles will not coalesce. Still, such merging yields 2D nanoflakes, but with a large variety in shapes (see Figure S5, Supporting Information). Additionally, we observe the formation of bulky 3D InSb nanostructures without a recurrent well-defined morphology (see Figure S5, Supporting Information). For these reasons, the 2D nanoflakes originating from a tip-to-sidewall collision and the 3D bulky nanostructures have not been considered in our study. We estimate that our growth platform yields a tip-to-tip collision with coalescence of the Au seed particle in more than 50% of the merging events. In all the other cases, we observe a tip-to-sidewall collision or the formation of a 3D bulky nanostructure. More information about the estimation can be found in Section S2 (Supporting Information).

A total of 12 nanoflakes are studied by TEM (see Section S3 Supporting information). The analysis of the TEM data yields four main results. First, all nanoflakes have only one Au seed particle. Therefore, we conclude that in all cases a tip-to-tip collision is followed by coalescence of the two Au seed particles. Second, all nanoflakes exhibit the zincblende crystal phase. Third, all nanoflakes predominantly grow in the plane formed by the two nanowires after merging and their large side facets are the stable {220} facets. Fourth, the nanoflakes show three recurrent grain boundaries arrangements dividing InSb single-crystalline domains, which allow us to categorize them in three distinct groups. We define the three groups of nanoflakes as “type-I”, “type-II”, and “type-III” and their internal structures as well as the resulting morphologies will be discussed in detail below.

Figure 2a–c shows representative Bright Field TEM (BF-TEM) images of each type of nanoflake. The original positions of the two merged nanowires can be traced back by following the extension of the InP stems, highlighted by white dotted lines and considering that the nanowires grow along opposite <111>B directions, thus forming an angle of  $109.4^\circ$ . These geometrical considerations allow us to identify the position where the two nanowires originally met in every nanoflake, which we will refer to as “merging area”. The nanoflake type can be unambiguously determined by looking at the lattice orientations in the merging area, while the morphological differences between the three types can be spotted by looking at their widening with respect to the two original InSb nanowires.

Figure 2d displays a representative high angle annular dark field scanning transmission electron microscopy (HAADF-STEM) image of the merging area

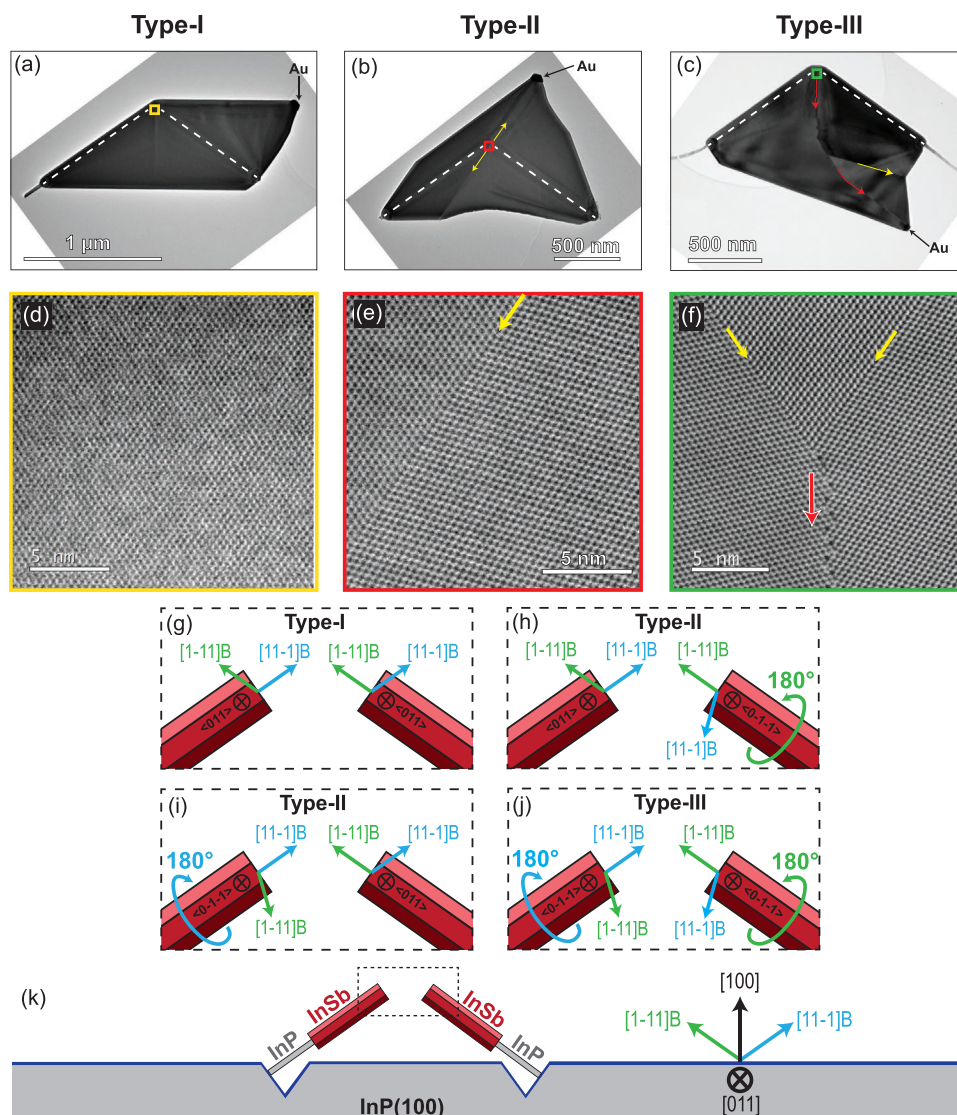


**Figure 2.** Relation between the crystal orientations of the three types of InSb nanoflakes and their final morphology. Panels a–c) are BF-TEM images of a) type-I, b) type-II, and c) type-III nanoflakes. The original direction of the two merged InSb nanowires is highlighted by the white dotted lines, while the squares indicate the merging area. The black arrows point to the positions of the Au seed particles. The presence of grain boundaries in b) type-II and c) type-III nanoflakes is discernible due to the diffraction contrast. Panels d–f) show HAADF-STEM images of the merging of d) type-I, e) type-II, and f) type-III nanoflakes, respectively. e) Type-II nanoflakes have only one  $\Sigma 3$  grain boundary, indicated by the yellow arrow, while type-III nanoflakes contain both  $\Sigma 3$  and  $\Sigma 9$  boundaries highlighted by the yellow and red arrows, respectively. The sketches in Panels g–j) are oriented along the  $\langle 011 \rangle$  direction and show the 4 possible merging orientations of the two original nanowires depending on their relative  $\langle 111 \rangle$ B directions. The sketch in k) shows the orientation of the substrate and the two  $\langle 111 \rangle$ B directions.

of a type-I nanoflake. Selected area electron diffraction patterns acquired from different areas on the nanoflake reveal a single-crystalline, defect-free InSb zincblende crystal (see Figure S7, Supporting Information). Type-I nanoflakes extend both upward and downward with respect to the original nanowire positions, with predominant growth perpendicular to one of the InSb nanowires.

In contrast to type-I nanoflakes, type-II and type-III nanoflakes have grain boundaries that divide the nanoflakes in multiple single-crystalline InSb domains. The presence of grain boundaries in type-II and type-III nanoflakes is visible in Figure 2b,c due to diffraction contrast. Figures S8 and S9

(Supporting Information) shows selected area diffraction patterns of different regions of these two types of nanoflakes. The HAADF-STEM image in Figure 2e shows the merging area of a type-II nanoflake. A twin boundary parallel to a  $\{111\}$ B plane is visible (see yellow arrow) and is classified as a “ $\Sigma 3$  grain boundary” according to the Coincident Site Lattice (CSL) terminology. The  $\Sigma 3$  boundary is formed during the merging event and extends both upward and downward along the common  $\{111\}$ B plane of the two single-crystalline InSb domains.

A representative HAADF-STEM image of the merging area of a type-III nanoflake is shown in Figure 2f. Three single-crystalline InSb domains are visible, separated by two twin

boundaries ( $\Sigma 3$  grain boundaries) directed along two opposite  $\{111\}$ B planes (yellow arrows) and one grain boundary characterized by a “zig-zag” behavior, which is a  $\Sigma 9$  grain boundary (red arrow). The growth history of the grain boundaries in the merging area of type-III nanoflakes and the order by which they develop cannot be fully explained from the data available. However, we infer that the nanowire collision occurs in the area located between the two  $\Sigma 3$  grain boundaries (see Figure S10, Supporting Information). Based on the position of the original nanowires, Type-III nanoflakes extend only downward along the  $\Sigma 9$  grain boundary. The direction of the  $\Sigma 9$  grain boundary is vertical for a few hundred nanometers and exhibits a zig-zag behavior until an additional  $\Sigma 3$  grain boundary is formed. At that point, the  $\Sigma 3$  grain boundary extends laterally, with the formation of a new single-crystalline InSb domain between the  $\Sigma 9$  and the newly formed  $\Sigma 3$  grain boundary. Additional TEM data on the grain boundaries of type-III nanoflakes can be found in Figures S11 and S12 (Supporting Information).

Type-I nanoflakes have the Au seed particle laying on the edge of the predominant grown side (Figure 2a). In the type-II case, the Au seed particle always lays on the top edge of the  $\Sigma 3$  grain boundary (Figure 2b). Interestingly, the position of the Au seed particle in type-III nanoflakes is at the bottom edge of the  $\Sigma 9$  grain boundary, implying that the Au particle “flips down” during the merging event (Figure 2c).

The formation of the three peculiar types of nanoflakes can be explained by considering the possible individual orientations of the two merging InSb nanowires. InSb nanowires grow epitaxially on top of InP nanowire stems, which are epitaxially connected to the InP substrate. Nevertheless, these InP stems have multiple stacking faults perpendicular to the growth direction, as previously reported.<sup>[34]</sup> These stacking faults consist of rotational twins of the zincblende InP lattice, which cause the InP stem to continue growing with a  $180^\circ$  ( $360^\circ$ ) rotation of the crystal orientation around the nanowire axis for an odd (even) number of stacking faults in the InP stem, resulting in a twin (same) orientation with respect to the substrate. This crystal orientation is then transferred to the InSb nanowire that grows epitaxially and defect-free on it, preserving the same lattice orientation up to the merging event. As the InP wires grow on two opposite  $\{111\}$ B facets of a trench, and thus in two different  $\langle 111 \rangle$ B directions,  $180^\circ$  rotations around their nanowire axes are not equivalent symmetry operations. For instance, a  $180^\circ$  rotation of the InSb lattice around the  $[11-1]$ B direction (left wire) is not equivalent to a  $180^\circ$  rotation around the  $[1-11]$ B direction (right wire).

According to these considerations, the two merging InSb nanowires can meet with four possible relative orientations, as displayed in Figure 2g–j that provide the formation probability of each nanoflake type. Without (or with an even number of) twins in the InP wires, the two InSb nanowires have the same epitaxial orientation. When they merge, they form a single-crystalline nanoflake, which is the type-I case (Figure 2g). There are two possibilities where one nanowire has an odd number of twins (and is rotated by  $180^\circ$  around its own axis) while the other one has an even number of twins (and has the same orientation as the substrate). These two cases are equivalent by mirror symmetry and they both lead to the formation of a  $\Sigma 3$  grain boundary, thus a type-II nanoflake. The

two InSb nanowires in Figure 2h share the  $[1-11]$ B direction and thus the  $\Sigma 3$  grain boundary can develop perpendicular to it, forming a  $\Sigma 3\{1-11\}$ B boundary, as illustrated in Figure 2b,e. If both merging nanowires have an odd number of twins, they will form a  $\Sigma 9$  grain boundary and thus a type-III nanoflake (Figure 2j). This occurs because the two nanowires do not share a common  $\langle 111 \rangle$ B direction. The two upward  $\Sigma 3$  boundaries (yellow arrows in Figure 2f) are  $\Sigma 3\{1-11\}$ B and  $\Sigma 3\{11-1\}$ B grain boundaries. Their formation is possible with the growth of an InSb domain which shares the  $[11-1]$ B and  $[1-11]$ B directions with the two neighboring InSb domains. Following these considerations, if we consider an ensemble of merging nanowires, 25% of them will form type-I nanoflakes, 50% type-II nanoflakes, and 25% type-III nanoflakes.

The TEM analysis reveals a connection between the type of boundary and the morphology of the nanoflakes. Type-I resembles a trapezoid with the two bases parallel to the surface of the InP substrate (Figure 2a). Type-II nanoflakes show more than three sides but their average shape is a triangle with the bottom side parallel to the InP substrate (Figure 2b). The average shape of the type-III nanoflake is a kite with the two equally long upper sides and two differently long bottom sides (Figure 2c). These three distinct morphologies (trapezoid, triangle, kite) make the three types identifiable by SEM and thus easily selectable for further measurements (see Figures S5 and S6, Supporting Information).

We study the morphological evolution of the three types by investigating how nanobridges develop during the growth. A total of 9 nanobridges are analyzed by TEM, revealing two type-I, three type-II and four type-III nanobridges according to their crystal quality. Figure 3a–c shows representative HAADF-STEM images of each type of nanobridges.

Type-I nanobridges (Figure 3a) show an in-plane extension of their shape using two separate growth modes. At the top part of the bridge, the catalyst particle lies either on the right or on the left of the merging point of the nanowires. Here, growth is most likely dominated by VLS growth. We observe that the VLS growth leads to an overall movement of the Au seed particle along the  $[0-11]$  or  $[01-1]$  direction respectively, depending on whether the Au particle was on the  $\{1-11\}$ B or  $\{11-1\}$ B facets after the merging event (Figure 3d; Figure S13, Supporting Information). At the bottom of the merging area, the concave edge benefits from the so-called re-entrant corner effect during subsequent Vapor-Solid (VS) growth: an enhanced growth rate at a location with a high density of kink sites as compared to that on flat facets.<sup>[36,37]</sup> The enhanced growth rate at the bottom edges causes the formation of four new smooth  $\{220\}$  facets, resulting in an overall downward widening. This layer-by-layer VS growth on these facets continues, forming also other smooth InSb facets different from  $\{220\}$  (see Figures S13–S15, Supporting Information) until the concave edge disappears.

The type-II nanobridge case is reported in Figure 3b,e. The Au seed particle lies on the top-edge of the  $\Sigma 3$  boundary and wets both InSb single-crystalline domains on different side facets (see Figure S14, Supporting Information). The nucleation at the VLS point of the Au seed particle initializes InSb layer-by-layer growth along the two side facets of the nanoflakes that belong to different single-crystalline domains. This result in an overall upward movement of the Au particle, always following

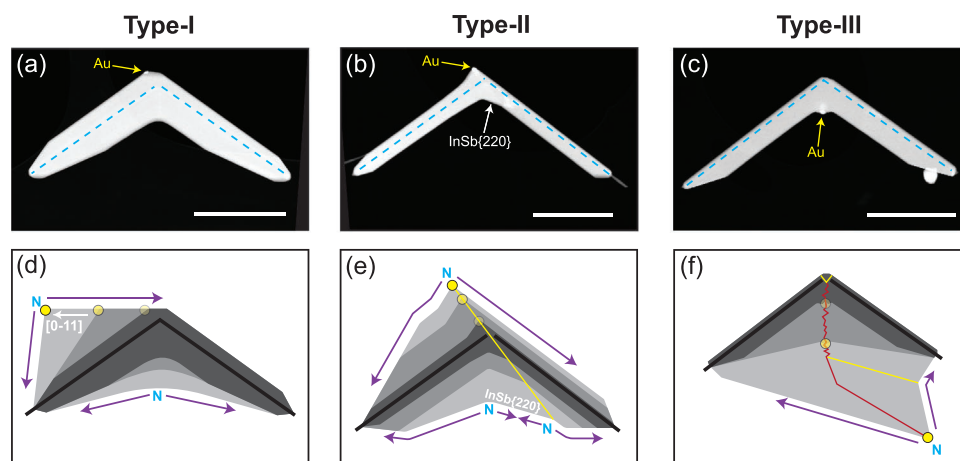


**Figure 3.** Morphology evolution of the three types of InSb nanoflakes. Panels a–c) are HAADF-STEM images of a) type-I, b) type-II, and c) type-III nanobridges. The positions of the two original InSb nanowires are indicated by the blue dotted lines. The yellow arrows point to the positions of the Au catalyst particles. All scale bars are 1  $\mu\text{m}$ . The sketches in Panels d–f) explain the morphology evolution of the three nanoflake types by starting from the nanobridges shown in Panels a–c), respectively. The black lines correspond to the original InSb nanowires. The nanoflakes at different stages of the growth are depicted by different tones of grey, with the time evolution indicated by moving from dark grey to light grey. The movement of the Au seed particle (yellow circle) is illustrated by using transparency, where a more transparent particle is associated with an earlier stage of the growth. The favorable nucleation points are marked with the letter “N”, while the purple arrows indicate the direction of layer-by-layer InSb growth along the side facets of the nanoflake.  $\Sigma 3$  and  $\Sigma 9$  grain boundaries are depicted as yellow and red lines respectively.

the direction of the  $\Sigma 3$  grain boundary, and an overall upward widening of the nanobridge. At the bottom, the increased re-entrant corner growth rate leads to a filling up of the concave area, as in the type-I case. In type-II nanoflakes, the concave area is formed by two concave edges separated by two InSb{220} side facets (both inclined to the viewing direction): one is the bottom edge of the  $\Sigma 3$  grain boundary while the other is the downward extension of the merging area (Figure 3e).

The type-III nanobridge case is shown in Figure 3c. The absence of the Au seed particle on top of type III nanoflakes implies that none of the two available leading growth mechanisms (VLS growth and VS growth at re-entrant corners) will initiate any upward growth. On the bottom, the Au particle is always on a concave bottom edge of the nanobridge, which coincides with the bottom end of the  $\Sigma 9$  grain boundary. The Au particle is always wetting both InSb domains divided by the  $\Sigma 9$  boundary (see Figures S11 and S15, Supporting Information). The presence of the Au catalyst particle yields a downward VLS growth. The nucleation from the Au seed particle initializes the lateral InSb layer-by-layer growth along the bottom side facets of the two InSb single-crystalline domains divided by the  $\Sigma 9$  grain boundary (Figure 3f). Moreover, in this case the growth can continue even after that the concavity has disappeared thanks to the catalytic effect of the Au particle. Therefore, a convex edge can be formed for longer growth times.

To determine whether the presence of  $\Sigma 3$  and  $\Sigma 9$  boundaries impacts the electronic properties of the nanoflakes, we study the electronic transport across the  $\Sigma 3$  and  $\Sigma 9$  boundaries of type-II and type-III nanoflakes and compare it to that of single-crystalline type-I nanoflakes. A total of eight nanoflake devices are fabricated. Nanoflakes are transferred by a micromanipulator to a p-doped Si/SiO<sub>x</sub> that acts as a local back-gate and allows for tuning of the applied back-gate voltage ( $V_{\text{bg}}$ ). Electron Back Scattered Diffraction (EBSD) is used to unambiguously determine the nanoflake type and to precisely locate their

grain boundaries, revealing two type-I, two type-II, and four type-III nanoflakes. Devices with two-terminal aluminum (Al) electrodes are fabricated such that electronic transport in type-I nanoflakes and across the boundaries of type-II and type-III nanoflakes can be studied via gate-tunable magnetoresistance performed at  $\approx 10$  mK. A representative image of the device configuration for each type is shown in the inset of Figure 4a–c, where the dashed yellow and red lines mark the direction of the  $\Sigma 3$  and  $\Sigma 9$  grain boundaries, respectively. The eight nanoflake devices are D1, D2... D8, where D1 and D2 are type-I, D3 and D4 are type-II, and D5–8 are type-III. The SEM images of all the eight devices are shown in Figures S16–S18 (Supporting Information), and the details of the device fabrication procedure and the EBSD analysis can be found in Section S4 (Supporting information).

The results of the electronic transport experiments are displayed in Figure 4. Figure 4a–c shows the two-terminal conductance ( $dI/dV$ ) as a function of back-gate voltage,  $V_{\text{bg}}$ , and the out-of-plane magnetic field,  $B$ , for a type-I (D1), a type-II (D3), and a type-III (D5) nanoflake device. The insets show the top-view false color SEM images of each device, with the dashed lines indicating the grain boundaries. Line scans of each plot at constant magnetic fields of 4 T, 8 T, and 11 T are shown in Figure 4d,f. The line scans of the type-I and type-II nanoflake devices resolve the first conductance plateaus at  $e^2/h$ , with plateaus length proportional to the applied magnetic field due to the Zeeman splitting. We estimate the effective Landé g-factor for D1 to be  $\approx |48|$  (see Section S4 and Figure S21 Supporting Information), in close agreement with the Landé g-factor of bulk InSb.<sup>[38]</sup> The possibility to resolve conductance plateaus in type-II nanoflakes indicates that the  $\Sigma 3$  grain boundary is not detrimental for the transport properties. Conversely, the type-III nanoflake device does not show any conductance plateaus even up to 11 T, possibly due to the presence of the  $\Sigma 9$  grain boundary. These results point to the more detrimental effect of

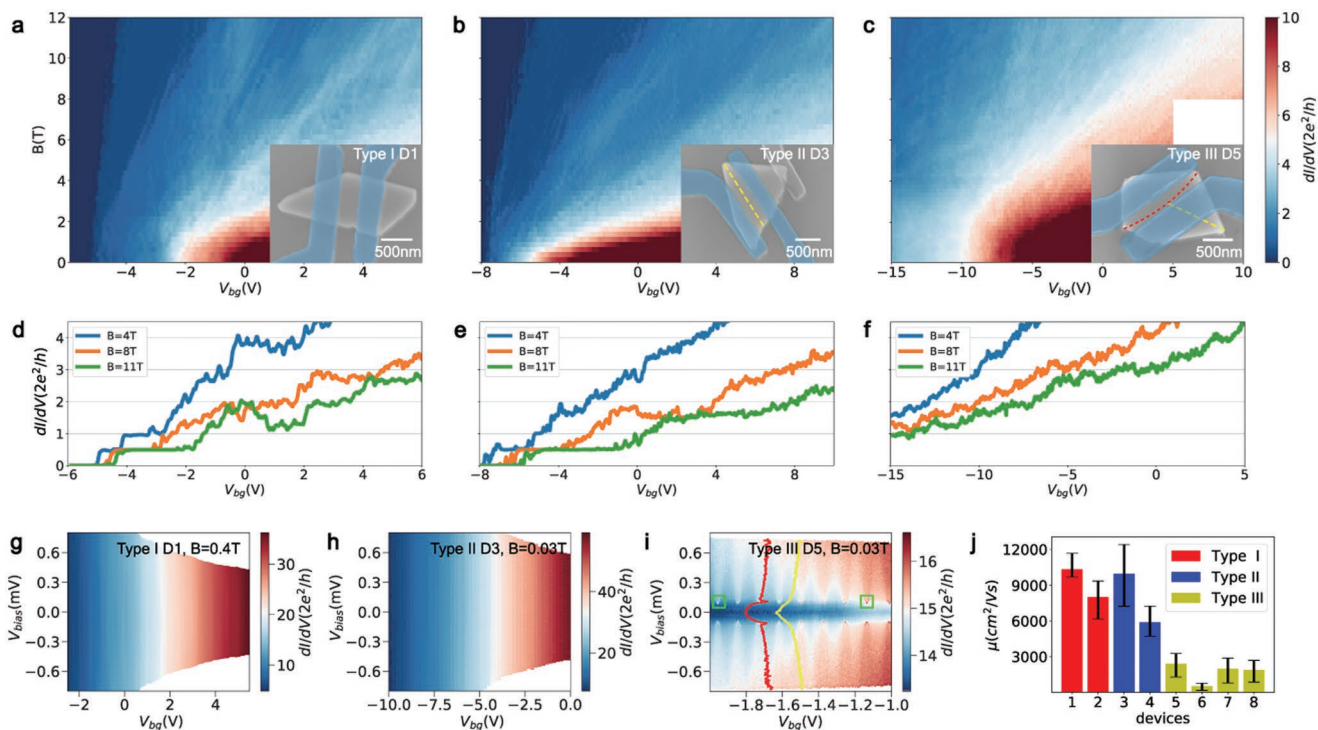


**Figure 4.** Electrical transport measurement at low temperature of the three types of nanoflakes. Panels a–c) show the two-terminal conductance as a function of back-gate voltage,  $V_{bg}$ , and magnetic field,  $B$ , (Landau-fan diagram) of a) Type I, b) Type II, and c) Type III nanoflakes. The insets display false color SEM images of the devices. The nanoflakes are contacted by Al electrodes (blue), with the  $\Sigma 3$  and  $\Sigma 9$  grain boundaries marked with yellow and red dashed-lines, respectively. d–f) are linecuts of the fan diagrams in a–c) at 4 T, 8 T, and 11 T, as indicated in the legends. g–i) are differential conductance,  $dI/dV$ , as a function of  $V_{bias}$  and  $V_{bg}$  of three types at the denoted low  $B$ -field. j) Field-effect mobility of the eight devices fabricated from three different type of nanoflakes.

the  $\Sigma 9$  grain boundary on the electronic transport compared to the  $\Sigma 3$  grain boundary.

Differential conductance ( $dI/dV$ ) measurements as a function of  $V_{bg}$  and small  $V_{bias}$  are performed on the three nanoflake device types and the results are shown in Figure 4g–i, respectively. The measurements are done at low magnetic fields (<0.5 T) which suppress superconductivity of the Al contacts (see Figure S20, Supporting Information) and that are too small to form detectable Landau levels. Both type-I and type-II devices show constant conductance for a given  $V_{bg}$  (Figure 4g,h). Moreover, the constant differential conductance as a function of  $V_{bias}$  at different  $V_{bg}$  indicates Ohmic behavior. In contrast, the type-III nanoflake device exhibits a persistent, symmetric conductance dip at zero-bias (Figure 4i). A conductance dip around zero-bias ( $\pm 0.1$  mV), and its persistence as a function of  $V_{bg}$  indicates that it is not due to random scattering, but could be attributed to the  $\Sigma 9$  grain boundary. In this case, the  $\Sigma 9$  grain boundary is generating an energy barrier on the order of 0.1 mV in type-III nanoflakes.<sup>[39]</sup> This energy barrier value is also consistent with the temperature of  $\approx 0.5$  K at which it disappears in a temperature sweep measurement, as shown in Figure S23 (Supporting Information). The conductance dip is not present in type-II devices (Figure 4h). In fact, type-II nanoflakes do not show substantial deviation from the transport in single-crystalline, type-I nanoflakes, which could be explained by the structural differences between the  $\Sigma 9$  and the  $\Sigma 3$  grain boundary. In addition, we measure regular conductance oscillations as a

function of  $V_{bg}$  and  $V_{bias}$  for the type-III nanoflake device D5, which gradually disappear above 1.6 K (see Figure S23, Supporting Information). The red and yellow lines of Figure 4i are taken at two values for  $V_{bg}$ : the red one coincides with an oscillation peak while the yellow one is taken in between two oscillation peaks. The measured oscillation peaks around the conductance dip seem to resemble Fabry–Pérot interference, where the  $\Sigma 9$  grain boundary constitutes an energy barrier at which the electrons are either reflected or transmitted and supports that the location of the  $\Sigma 9$  grain boundary is in between the two contacts (see Figure S18b, Supporting Information). Two representative oscillation peaks are framed by green squares in Figure 4i to highlight that these peaks consistently occur at the edge of the conductance dip. We note that these oscillation peaks have only been measured in one device (D5), however the dip in conductance around zero bias has also been measured in another type-III device (D6), albeit the oscillation peaks were not resolvable (see Figure S22d, Supporting Information). The unresolvable oscillation peaks could possibly be attributed to a longer contact spacing or a different thickness in device (D6), whose SEM image is shown in Figure S18c (Supporting Information). The other two type-III nanoflake devices (D7 and D8) were not measured and were used only for the field-effect transistor (FET) mobility experiments.

FET mobility measurements are performed on all the 8 nanoflake devices (see Figure S19, Supporting Information) and the extracted mobility values for each device are displayed

in the histogram plot of Figure 4j. A detailed explanation of the FET mobility extraction can be found in Section S4 (Supporting Information). Type-I and type-II nanoflake devices show similar mobility values in the range of 6000–10 000 cm<sup>2</sup> V<sup>-1</sup> s<sup>-1</sup>, in agreement with previous studies on free-standing InSb 2D nanostructures.<sup>[26–28,30,40]</sup> On the other hand, type-III nanoflake devices have a mobility of about three times lower compared to type-I and type-II. This result further supports a possible detrimental effect of the transport properties due to the presence of the  $\Sigma 9$  grain boundary.

To summarize, our transport results provide a preliminary study on the effect of  $\Sigma 3$  and  $\Sigma 9$  grain boundaries on the electron transport in InSb nanoflakes, suggesting that a  $\Sigma 9$  grain boundary behaves as a potential energy barrier. Such a grain boundary in topological system is predicted to host interacting electronic modes and behave as an exotic 1D quantum wire.<sup>[41]</sup> Conversely, electron transport across a  $\Sigma 3$  grain boundary seems to be comparable to the single-crystalline nanoflakes and thus indicating the minimal effect of the  $\Sigma 3$  grain boundary on the transport properties.

### 3. Conclusion

This paper provides a detailed study of the crystal structure and formation dynamics of InSb nanoflakes via the merging of two InSb nanowires grown on an InP platform, which was possible thanks to the limited thickness achieved with our growth technique. Depending on the individual orientation of the merging nanowires, three types of InSb nanoflakes are possible. Type-I nanoflakes are single crystalline, type-II nanoflakes contain a  $\Sigma 3$  grain boundary, and type-III nanoflakes contain a  $\Sigma 9$  grain boundary and  $\Sigma 3$  grain boundaries, granting each type of nanoflake a distinct morphology. Rotational twins along the InP stems give rise to the different merging possibilities and thus the different types of nanoflakes. Electronic transport studies suggest that a  $\Sigma 9$  grain boundary is detrimental for possible quantum devices. However, this boundary can potentially be exploited to host interacting electronic modes and behave as an exotic 1D quantum wire in topological system. The type-I and type-II nanoflakes show promising transport properties, rendering them useful for quantum devices.

The high level of control enabled by our growth technique can be exploited for the fabrication of complex hybrid semiconductor-superconductor quantum devices via a directional superconductor deposition. Compared to previous methods for the VLS growth of free-standing InSb 2D nanostructures, smart inter-shadowing between the InSb nanoflake and crossed nanowire networks is possible, and all have a pre-determined position and orientation in the space. As an example, using the same design displayed in Figure S3a (Supporting Information), a 4-terminal Josephson junction can be created by shadowing a nanowire cross on a InSb nanoflake, and can be used to study novel topological properties.<sup>[42]</sup> The possibility to accommodate multiple nanostructures and thus shadowing geometries on the same chip makes this technique rather flexible for designing quantum devices.

### Supporting Information

Supporting Information is available from the Wiley Online Library or from the author.

### Acknowledgements

The authors thank Peterus Johannes van Veldhoven for the support with the MOVPE reactor at the Eindhoven University of Technology and Yigitcan Uzun for insightful discussions. The authors thank NanoLab@TU/e for their help and support. Solliance and the Dutch province of Noord-Brabant are acknowledged for funding the TEM facility. This work was supported by the Dutch Research Council (NWO), grant codes TOP.016.001 and TK11812P04. The work of Z.Y.Z., G. Y., G.L., J.Y.S., L.L., and J.S. were supported by the National Natural Science Foundation of China (Grant Nos. 92065203 and 12174430), the Strategic Priority Research Program B of Chinese Academy of Sciences (Grant No. XDB33000000), the Beijing Nova Program (Grant No. Z211100002121144), and the Synergetic Extreme Condition User Facility (SECUF).

### Conflict of Interest

The authors declare no conflict of interest.

### Author Contributions

M.R., G.B., S.G., and R.L.M.O.H.V. fabricated the platform for the nanowire growth and carried out the InSb nanoflakes growth. M.R. and R.L.M.O.H.V. did the nanoflake manipulation for the TEM analysis. M.V.A. performed the TEM analysis. M.A.V., G.B., and E.P.A.M.B. provided key suggestions and discussions for the understanding of the TEM analysis and the nanoflake growth dynamics. E.P.A.M.B. and M.A.V. supervised the growth experiments. Z.Y.Z., G.Y., G.L., and J.Y.S. fabricated the nanoflake devices and performed the transport measurements. Z.Y.Z., G.Y., G.L., J.Y.S., L.L., and J.S. analyzed the transport data. L.L., and J.S. supervised the transport experiments. M.R. wrote the manuscript with inputs from all co-authors.

### Data Availability Statement

The data that support the findings of this study are openly available in Zenodo at <https://doi.org/10.5281/zenodo.7152756>, reference number 7152756.

### Keywords

electronic transports, InSb, metal organic vapor phase epitaxy, nanoflakes, nanowires

Received: October 17, 2022

Revised: December 28, 2022

Published online:

[1] K. Takase, K. Tateno, S. Sasaki, *Appl. Phys. Express* **2019**, *12*, 117002.

[2] Z. Yang, B. Heischmidt, S. Gazibegovic, G. Badawy, D. Car, P. A. Crowell, E. P. A. M. Bakkers, V. S. Pribiag, *Nano Lett.* **2020**, *20*, 3232.

- [3] H. Chen, N. Xi, K. W. C. Lai, C. K. M. Fung, R. Yang, presented at *2009 IEEE Nanotechnology Materials and Devices Conf.*, XX, Traverse City, MI June 2009.
- [4] C. J. Goosney, V. M. Jarvis, D. P. Wilson, N. I. Goktas, R. R. LaPierre, *Semicond. Sci. Technol.* **2019**, *34*, 035023.
- [5] S. Zhang, H. Jiao, X. Wang, Y. Chen, H. Wang, L. Zhu, W. Jiang, J. Liu, L. Sun, T. Lin, H. Shen, W. Hu, X. Meng, D. Pan, J. Wang, J. Zhao, J. Chu, *Adv. Funct. Mater.* **2020**, *30*, 2006156.
- [6] J. W. G. Van den Berg, S. Nadj-Perge, V. S. Pribiag, S. R. Plissard, E. P. A. M. Bakkers, S. M. Frolov, L. P. Kouwenhoven, *Phys. Rev. Lett.* **2013**, *110*, 066806.
- [7] N. Mingo, *Appl. Phys. Lett.* **2004**, *84*, 2652.
- [8] M. T. Deng, C. L. Yu, G. Y. Huang, M. Larsson, P. Caroff, H. Q. Xu, *Nano Lett.* **2012**, *12*, 6414.
- [9] I. Van Weperen, B. Tarasinski, D. Eeltink, V. S. Pribiag, S. R. Plissard, E. P. A. M. Bakkers, L. P. Kouwenhoven, M. Wimmer, *Phys. Rev. B* **2015**, *91*, 201413.
- [10] J. E. Sestoft, T. Kanne, A. N. Gejl, M. von Soosten, J. S. Yodh, D. Sherman, B. Tarasinski, M. Wimmer, E. Johnson, M. Deng, J. Nygård, T. S. Jespersen, C. M. Marcus, P. Krogstrup, *Phys. Rev. Mater.* **2018**, *2*, 044202.
- [11] R. M. Lutchny, E. P. A. M. Bakkers, L. P. Kouwenhoven, P. Krogstrup, C. M. Marcus, Y. Oreg, *Nat. Rev. Mater.* **2018**, *3*, 52.
- [12] F. Qu, J. van Veen, F. K. de Vries, A. J. A. Beukman, M. Wimmer, W. Yi, A. A. Kiselev, B.-M. Nguyen, M. Sokolich, M. J. Manfra, F. Nichele, C. M. Marcus, L. P. Kouwenhoven, *Nano Lett.* **2016**, *16*, 7509.
- [13] T. Masuda, K. Sekine, K. Nagase, K. S. Wickramasinghe, T. D. Mishima, M. B. Santos, Y. Hirayama, *Appl. Phys. Lett.* **2018**, *112*, 192103.
- [14] C. T. Ke, C. M. Moehle, F. K. de Vries, C. Thomas, S. Metti, C. R. Guinn, R. Kallaher, M. Lodari, G. Scappucci, T. Wang, R. E. Diaz, G. C. Gardner, M. J. Manfra, S. Goswami, *Nat. Commun.* **2019**, *10*, 3764.
- [15] C. M. Moehle, C. T. Ke, Q. Wang, C. Thomas, D. Xiao, S. Karwal, M. Lodari, V. van de Kerkhof, R. Termaat, G. C. Gardner, G. Scappucci, M. J. Manfra, S. Goswami, *Nano Lett.* **2021**, *21*, 9990.
- [16] K. J. Goldammer, S. J. Chung, W. K. Liu, M. B. Santos, J. L. Hicks, S. Raymond, S. Q. Murphy, *J. Cryst. Growth* **1999**, *201*, 753.
- [17] N. Goel, J. Graham, J. C. Keay, K. Suzuki, S. Miyashita, M. B. Santos, Y. Hirayama, *Phys. E* **2005**, *26*, 455.
- [18] W. Yi, A. A. Kiselev, J. Thorp, R. Noah, B.-M. Nguyen, S. Bui, R. D. Rajavel, T. Hussain, M. F. Gyure, P. Kratz, Q. Qian, M. J. Manfra, V. S. Pribiag, L. P. Kouwenhoven, C. M. Marcus, M. Sokolich, *Appl. Phys. Lett.* **2015**, *106*, 142103.
- [19] C. A. Lehner, T. Tschirky, T. Ihn, W. Dietsche, J. Keller, S. Fält, W. Wegscheider, *Phys. Rev. Mater.* **2018**, *2*, 054601.
- [20] S.-I. Gozu, K. Akahane, N. Yamamoto, A. Ueta, *J. Vac. Sci. Technol., B: Microelectron. Nanometer Struct. Process., Meas., Phenom.* **2006**, *24*, 2291.
- [21] Z. Lei, C. A. Lehner, E. Cheah, C. Mittag, M. Karalic, W. Wegscheider, K. Ensslin, T. Ihn, *Phys. Rev. Res.* **2021**, *3*, 023042.
- [22] D. J. Carrad, M. Bjergfelt, T. Kanne, M. Aagesen, F. Krizek, E. M. Fiordaliso, E. Johnson, J. Nygård, T. S. Jespersen, *Adv. Mater.* **2020**, *32*, 1908411.
- [23] S. A. Khan, C. Lampadaris, A. Cui, L. Stampfer, Y. Liu, S. J. Pauka, M. E. Cachaza, E. M. Fiordaliso, J.-H. Kang, S. Korneychuk, T. Mutas, J. E. Sestoft, F. Krizek, R. Tanta, M. C. Cassidy, T. S. Jespersen, P. Krogstrup, *ACS Nano* **2020**, *14*, 14605.
- [24] M. Pendharkar, B. Zhang, H. Wu, A. Zarassi, P. Zhang, C. P. Dempsey, J. S. Lee, S. D. Harrington, G. Badawy, S. Gazibegovic, R. L. M. Op Het Veld, M. Rossi, J. Jung, A.-H. Chen, M. A. Verheijen, M. Hocevar, E. P. A. M. Bakkers, C. J. Palmström, S. M. Frolov, *Science* **2021**, *372*, 508.
- [25] S. Heedt, M. Quintero-Pérez, F. Borsoi, A. Fursina, N. van Loo, G. P. Mazur, M. P. Nowak, M. Ammerlaan, K. Li, S. Korneychuk, J. Shen, M. A. Y. van de Poll, G. Badawy, S. Gazibegovic, N. de Jong, P. Aseev, K. van Hoogdalem, E. P. A. M. Bakkers, L. P. Kouwenhoven, *Nat. Commun.* **2021**, *12*, 4914.
- [26] M. De La Mata, R. Leturcq, S. R. Plissard, C. Rolland, C. Magén, J. Arbiol, P. Caroff, *Nano Lett.* **2016**, *16*, 825.
- [27] D. Pan, D. X. Fan, N. Kang, J. H. Zhi, X. Z. Yu, H. Q. Xu, J. H. Zhao, *Nano Lett.* **2016**, *16*, 834.
- [28] S. Gazibegovic, G. Badawy, T. L. J. Buckers, P. Leubner, J. Shen, F. K. de Vries, S. Koelling, L. P. Kouwenhoven, M. A. Verheijen, E. P. A. M. Bakkers, *Adv. Mater.* **2019**, *31*, 1808181.
- [29] I. Verma, V. Zannier, F. Rossi, D. Ercolani, F. Beltram, L. Sorba, *Nanotechnology* **2020**, *31*, 384002.
- [30] I. Verma, S. Salimian, V. Zannier, S. Heun, F. Rossi, D. Ercolani, F. Beltram, L. Sorba, *ACS Appl. Nano Mater.* **2021**, *4*, 5825.
- [31] S. A. Khan, L. Stampfer, T. Mutas, J.-H. Kang, P. Krogstrup, T. S. Jespersen, *Adv. Mater.* **2021**, *33*, 2100078.
- [32] C. Caneau, R. Bhat, M. Koza, J. R. Hayes, R. Esagui, *J. Cryst. Growth* **1991**, *107*, 203.
- [33] D. Dalacu, A. Kam, D. G. Austing, P. J. Poole, *Nano Lett.* **2013**, *13*, 2676.
- [34] D. Car, J. Wang, M. A. Verheijen, E. P. A. M. Bakkers, S. R. Plissard, *Adv. Mater.* **2014**, *26*, 4875.
- [35] S. Gazibegovic, Bottom-up grown InSb nanowire quantum devices, Ph.D. Thesis, Eindhoven University of Technology, Eindhoven **2019**.
- [36] P. Hartman, *Z. Kristallogr. - Cryst. Mater.* **1956**, *107*, 225.
- [37] R. S. Wagner, *Acta Metall.* **1960**, *8*, 57.
- [38] O. Madelung, in *Semiconductors: Data Handbook*, Springer, Berlin, Heidelberg **2004**, pp. 71–172.
- [39] Y. Fu, M. Willander, in *Physical models of semiconductor quantum devices*, Springer, New York **1999**, pp. 194–196.
- [40] N. Kang, D. Fan, J. Zhi, D. Pan, S. Li, C. Wang, J. Guo, J. Zhao, H. Xu, *Nano Lett.* **2018**, *19*, 561.
- [41] M. T. Randeria, K. Agarwal, B. E. Feldman, H. Ding, H. Ji, R. J. Cava, S. L. Sondhi, S. A. Parameswaran, A. Yazdani, *Nature* **2019**, *566*, 363.
- [42] R.-P. Riwar, M. Houzet, J. S. Meyer, Y. V. Nazarov, *Nat. Commun.* **2016**, *7*, 11167.